Petroleum Science 23 (2026) 69–83

Contents lists available at ScienceDirect

Petroleum Science

journal homepage: www.keaipublishing.com/en/journals/petroleum-science

Original Paper

Organic and inorganic pore networks in medium- to low-maturity shale: Insights from SEM analysis of Shahejie Formation in the Dongying Sag

Zi-Zhi Lin [a,b], Qin-Hong Hu [a,c,*], Na Yin [a,b,**], Yu-Shan Du [d], Jing Chao [d], Guang-Lei Zhang [e], Song-Tao Wu [f]

[a] National Key Laboratory of Deep Oil and Gas, China University of Petroleum (East China), Qingdao, 266580, Shandong, China
[b] School of Geosciences, China University of Petroleum (East China), Qingdao, 266580, Shandong, China
[c] Laboratory for Marine Mineral Resource, Qingdao Marine Science and Technology Center, Qingdao, 266237, Shandong, China
[d] Exploration and Production Research Institute of Shengli Oilfield Company, Sinopec, Dongying, 257015, Shandong, China
[e] School of Civil and Transportation Engineering, Hebei University of Technology, Tianjin, 300401, China
[f] The Research Institute of Petroleum Exploration and Development, PetroChina, Beijing, 100083, China

ARTICLE INFO

Article history:
Received 10 January 2025
Received in revised form
28 June 2025
Accepted 9 September 2025
Available online 13 September 2025

Edited by Jie Hao and Xi Zhang

Keywords:
Dongying Sag
Shahejie Formation
Low-mature shale
Field emission scanning electron
Microscopy
Organic-inorganic pores
Two-dimensional porosity
Multiscale SEM imaging

ABSTRACT

The spatial distribution and structural characteristics of organic and inorganic pore networks are crucial for evaluating the storage capacity of medium- to low-maturity shale reservoirs. Based on scanning electron microscopy images of Shahejie Formation shales in the Dongying Sag, this study established an efficient, low cost, and reliable technical method for quantitatively analyzing the structural characteristics and geological control factors of organic and inorganic pores. Shales exhibit three main pore systems: (1) nanoscale intragranular pores in clay minerals, calcite, and pyrite; (2) nano- to micron-scale pores between mineral particles and organic-inorganic interface pores; and (3) micron-to millimeter-scale microfractures at the laminar interface. The number and surface porosity of organic and inorganic pores are highly correlated with the content of shale components. Organic pores in shales mostly exist in the form of organic-inorganic interface pores, with an average pore size of 600–800 nm, providing the surface porosity of 14.9%, which has an important influence on the development of submicron (200–1000 nm) scale pores. The number of inorganic pores contributes 91.45% of the total number of pores and accounts for 85.1% of the total surface porosity. The influence of clay mineral-related pores is the most significant in inorganic pores; it not only has a significant impact on the pores in the pore size range of 0–200 nm but also affects the development of micron-scale pores together with calcite. The fractal results show that the morphological complexity of inorganic pores is higher than that of organic pores. In addition, low-resolution images will greatly underestimate the contribution of nanoscale pores to the reservoir space. Therefore, the quantitative evaluation of dense porous media should comprehensively consider the weight of resolution and field of view. The results of this study provide important microstructural data for an in-depth understanding of the organic and inorganic pore structure characteristics of medium- and low-maturity shales, and for providing more accurate reservoir quality evaluation for shale resource exploration.

1. Introduction

The success of the shale oil revolution in the United States has attracted widespread attention to unconventional oil and gas resources represented by shale oil (Zou et al., 2020; Wang et al., 2021; Li et al., 2024; Lin et al., 2024a). The pore network of shale provides an important place and path for the storage and migration of oil and gas, so a comprehensive understanding of the pore

* Corresponding author.
** Corresponding author.
E-mail addresses: huqinhong@upc.edu.cn (Q.-H. Hu), 18306422290@163.com (N. Yin).

Peer review under the responsibility of China University of Petroleum (Beijing).

https://doi.org/10.1016/j.petsci.2025.09.018

system of shale reservoirs is the basis for evaluating the storage and flow mechanisms of hydrocarbons.

Previous researchers have conducted extensive and fruitful research on the spatial type and multi-scale pore structure of shale reservoirs through high-pressure mercury injection porosity, low-temperature nitrogen adsorption, nuclear magnetic resonance, and other technologies (Yang et al., 2016; Lin et al., 2022; Tian et al., 2022; Zhang et al., 2021; Zhao et al., 2020; Li et al., 2024). Loucks et al. (2009) first used scanning electron microscopy (SEM) to characterize the nature, formation, and distribution of nanoscale pores in the Barnett shale and found a large number of pores in organic particles with an internal porosity of up to 20.2%. This discovery has gradually attracted the attention of geologists to the role of organic pores in the reservoir space of shale. It is generally believed that the development of organic pores is affected by factors such as kerogen type, maturity, and thermal evolution history (Chalmers and Bustin, 2008; Curtis et al., 2012). Inorganic pores are more significantly affected by the composition of shale materials and diagenesis, and the reservoir space is mainly composed of intergranular pores between detrital minerals and intragranular pores of clay minerals (Slatt and O'Brien, 2011; Gao et al., 2020; Lin et al., 2024b). The organic-inorganic pores are interconnected to form a complex pore network channel, allowing oil and gas to migrate from the pores to the wellbore.

However, reports on organic pore characteristics are mainly focused on medium-to high-maturity shales, and systematic studies on organic pores in medium- to low-maturity shales are often neglected. It is generally believed that shales from low maturity to mature shale stages have no organic pores (Loucks et al., 2009, 2012; Curtis et al., 2012; Xiao et al., 2024). However, some scholars found that there are also a certain number of organic pores in the shale of low maturity when studying low-maturity shale. These pores mainly exist in the form of organic-inorganic interface pores, but no systematic reports have been found (Mathia et al., 2016; Zhang et al., 2019; Yang et al., 2022). In view of the key role of organic-inorganic pore systems in the storage and migration of oil and gas, it is necessary to conduct a systematic study of the organic-inorganic pore network in shale reservoirs at medium to low maturity stages.

In addition, the organic-inorganic pore structure in shale is mostly focused on the qualitative description of the morphological characteristics of the pores. Some studies have attempted to use threshold segmentation, edge detection and other algorithms to conduct quantitative analysis (Ma et al., 2016; Gao et al., 2020; Iqbal et al., 2021), but most of them are based on local areas and extrapolated to the overall structure, which is mainly applicable to relatively homogeneous marine shales. For lacustrine shales with significant vertical heterogeneity, it is more challenging to observe the overall pore structure, and manual methods are often inadequate. Although the wide field of view stitching technology has made breakthroughs in the observation range, it has problems such as long time consumption, high cost, and difficulty in distinguishing organic-inorganic pores, which limit its application. Therefore, it is urgent to develop an economical, efficient, fast, and comprehensive organic-inorganic pore structure characterization technology.

Given the current shortcomings and high costs in the identification and quantitative characterization of organic-inorganic pore networks in medium- and low-maturity shales, this study aims to propose an efficient, low-cost and reliable pore structure characterization method based on high-resolution scanning electron microscope images to achieve quantitative analysis of organic-inorganic pore networks in medium- and low-maturity shales. In addition, this paper also systematically compares the changes in pore structure parameters under different magnifications and explores the influence of imaging resolution on pore identification accuracy and network structure. This method was applied to the shale of the Shahejie Formation in the Dongying Sag, effectively revealing its organic-inorganic pore microstructure characteristics and, to a certain extent, clarifying the main geological control factors of pore development in medium- and low-maturity shales. The research results are helpful to improve the accuracy of reservoir quality evaluation of medium-to low-maturity shale oil, and provide technical support and theoretical basis for the optimization of exploration strategies.

2. Samples and methodologies

2.1. Samples and basic properties analyses

The eight shale samples in this study were collected from Well A in the Dongying Sag of the Bohai Bay Basin, China. Their burial depths range from 3539 to 3587 m and belong to E_s4^U. The inorganic minerals in the samples are mainly composed of quartz (16.03% ± 4.9%), calcite (25.2% ± 1.7%), dolomite (21.8% ± 9.9%), clay minerals (28.7% ± 7.7%), etc., accounting for a total proportion of about 91% ± 1.3% (Table 1). Fig. 1 shows the lithological ternary diagram of the samples. The lithologies of the eight shale samples can be divided into calcareous shale and mixed shale, which cover the main lithological types in the study area. The total organic carbon content ranges from 1.04% to 2.82%, with an average of 2.09%, demonstrating good oil generation potential. In addition, the organic matter type is mainly type II kerogen, and the pyrolysis peak temperature (T_{max}) ranges from 433 to 443 °C, indicating that the shale is in a low maturity stage.

During sample processing, these irregular shales were cut into 1 cubic centimeter blocks using diamond wire cutting, and the sections perpendicular to the bedding direction were further polished and coated for SEM observation to reduce shale heterogeneity and capture more pore structure characteristics of the laminated shales. Parallel samples are used for mineral composition analysis (XRD) and organic geochemical analysis, including TOC and rock pyrolysis, according to standard methods (Behar et al., 2001).

2.2. Methodologies

2.2.1. Scanning electron microscope experiment

SEM experiments were performed on a Helios NanoLab-650 focused ion beam-field emission SEM from FEI, USA, using back-scattered electron (BSE) imaging mode to collect images (accelerating voltage of 5 kV and accelerating current of 0.4 nA) to highlight pore morphology and composition contrast.

2.2.2. Image processing workflow

This study employed Avizo software (Thermo Fisher Scientific, USA) for multi-component identification and organic and inorganic pore segmentation and extraction. The workflow followed is outlined below (Fig. 1):

(1) To overcome the influence of shale heterogeneity and ensure the representativeness of the SEM images, a series of SEM images from different fields of view were stitched together to create high-resolution, large-field images that accurately represent the sample characteristics (Fig. 2(b)). The selection of image stitching regions should first avoid secondary fractures generated during the processing. In addition, considering that the laminar samples are the research objects, the characteristics of different laminae (clay-organic laminae and carbonate laminae) should be

Table 1
Mineral composition, TOC, maximum pyrolysis temperature, and kerogen type of eight shale samples.

Sample No.	Sample depth, m	Lithology division	TOC, %	T_{max}, °C	Kerogen type	Mineral composition, %							Relative content of clay minerals, %	
						Quartz	Feldspar	Calcite	Pyrite	Plaster	Dolomite	Clays	I/S	Illite
1	3542.74	I_0	2.15	442	II_B	12	2.9	40.4	4.7	0.6	25.5	13.9	49	51
2	3544.4	IV_1	2.82	437	I	14.6	5.2	24.2	4	0	20.9	31.1	54	46
3	3545.2	I_2	2.67	441	II_B	12.9	3.6	7.5	2.7	0	44.4	28.9	51	41
4	3549.12	I_2	2.04	441	I	11.6	7.1	33.3	0.9	0	18.7	28.4	56	41
5	3576.02	I_2	2.31	433	II_A	15.6	4	29.8	2.4	0	20.3	27.9	51	47
6	3580.2	IV_1	1.7	439	II_B	15.7	4	27.3	3.8	0.5	13.7	35.0	48	52
7	3585.03	IV_1	1.97	438	II_B	19.4	5.7	29.3	2.5	0.6	18.1	24.4	56	43
8	3587.5	IV_3	1.04	443	I	26.5	7.6	10.1	2.3	0.3	13.1	40.1	54	46

I/S: Proportion of illite-smectite mixed-layer minerals in clay minerals.

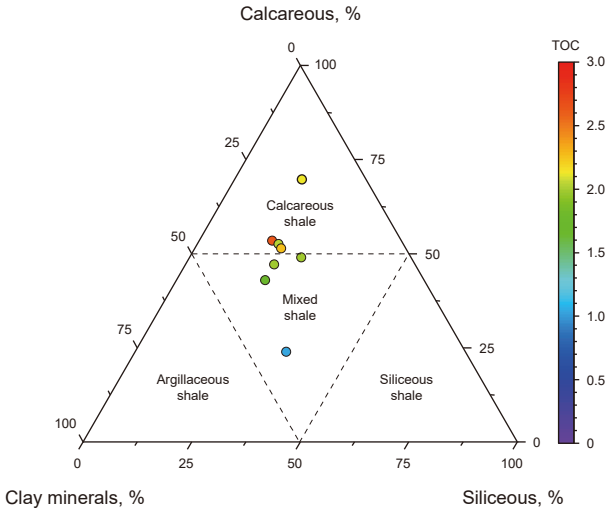

Fig. 1. Mineral ternary diagrams of eight shale samples.

included in the image selection, and the total number of images of different laminae should be greater than 6.

(2) The image regions of interest were cropped to remove edge artifacts and non-representative areas, and then a 3 × 3 median filter was used to remove salt stains while preserving pore-mineral boundaries, followed by Gaussian smoothing (10 pixels) to attenuate high-frequency noise while not blurring fine features.

(3) The pre-processed SEM images were binarized so that the image grayscale range was mapped to between 0 and 255. Interactive threshold segmentation was used to distinguish pores (darkest grayscale, between 0 and 48) and rock mineral matrix (organic matter between 49 and 100; quartz-clay, etc. Between 100 and 160; calcite between 160 and 180; other minerals between 180 and 230; pyrite between 230 and 255) using the bimodal intensity distribution as a guide, and corresponding labels were added (Fig. 2(c)). It should be noted that we selected typical mineral labeling areas and verified them in the EDS spectrum to ensure the accuracy of the labeling. Subsequently, the brightness difference filter map (gradient amplitude range of 40–255) was calculated using the Interactive Top-Hat algorithm to enhance the subtle contrast between mineral phases, to enhance the accuracy of the extraction of micropore structure. The combination of these algorithms can obtain more detailed and accurate pore structure information; then, the mineral and pore boundaries (image gradient) obtained based on the spatial variation rate of the image grayscale value are combined with the improved watershed algorithm (marker-based watershed) to optimize the boundaries and separate the regions of the labeled complex structures (pores, organic matter, pyrite, calcite, quartz-clay, etc.) to ensure that the seed region of each phase matches its characteristic grayscale range (Fig. 2(d) and (e)).

(4) The Expand Lables algorithm is used to expand the existing labeled regions (such as pores, organic matter, minerals, etc.) to a certain distance to the surrounding voxels, while keeping the non-overlap and clear boundaries between different labels to ensure that all voxels in the image have been completely labeled, thereby obtaining the optimized complete multiphase segmentation result; then the Dilation and Erosion algorithms (usually 1 voxel) are used to label the pore part to obtain the matching relationship between the pores and the mineral particles, and the label analysis, Volume Fraction and other commands are further used to calculate the correlation between the pores and the organic and inorganic mineral components, and quantitatively extract the structural parameters of different mineral pores.

Ultimately, twenty-four sets of large-field stitched SEM images, with varying resolutions, were identified from eight samples, covering a total field of view of approximately 220000 μm^2.

2.2.3. Pore topology parameters

Following the multiphase segmentation and identification process, several essential two-dimensional topological structural parameters of the pore spaces were delineated. These parameters encompass porosity, equivalent diameter, pore size distribution, and fractal dimension. Such parameters are pivotal for characterizing pore spaces and elucidating their connectivity within the material framework. This is crucial for advancing porous media studies, particularly in applications demanding precise porosity measurements and connectivity assessments.

The volumetric fraction parameter is employed to quantify surface porosity, representing the ratio of object pixels to total image pixels. This calculation method is described in Eq. (1):

$$\varphi = \frac{S_{PV}}{g_x \times g_y} \times 100\% = \frac{\sum_{y_i < g_y}^{x_i < g_x} S_i}{g_x \times g_y} \times 100\% \quad (1)$$

where $g_x \times g_y$ and S_{PV} respectively represent the number of voxels in the x and y-axis directions in the image; SPV corresponds to the number of voxels in the pore space.

The Crofton perimeter is utilized to measure the perimeter of a pore (Aili and Maruyama, 2020). For a square grid, the perimeter is

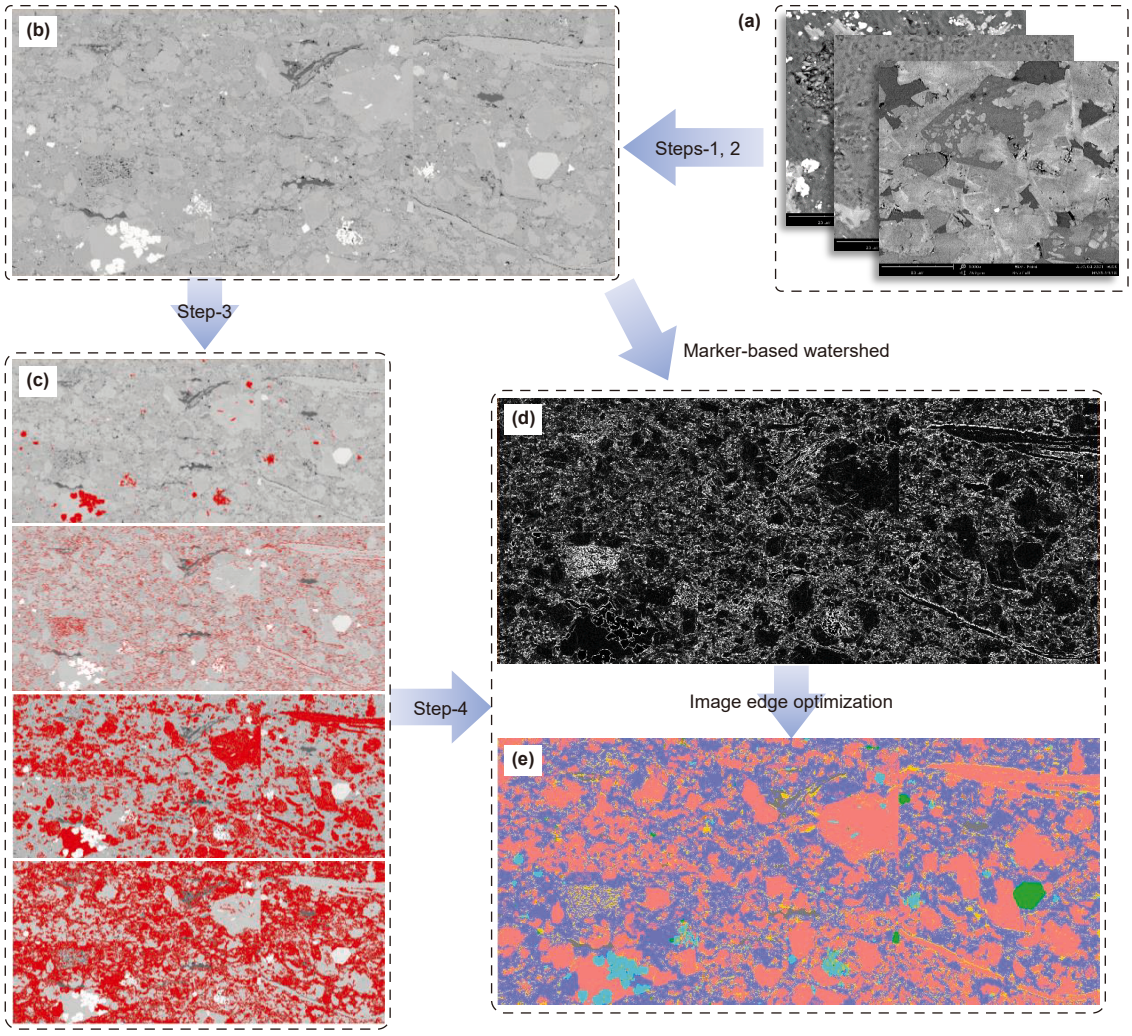

Fig. 2. Schematic diagram of the image processing workflow.

computed by summing the intercepts across the four principal directions:

$$L(X)=\int_0^x D_2(X,\alpha)\mathrm{d}\alpha=\frac{\pi}{4}\times\left(a\times(N_0+N_{90})+\frac{a}{\sqrt{2}}\times(N_{45}+N_{135})\right) \tag{2}$$

Here, a is the distance between two points on the grid and the distance between two lines in the 0° or 90° directions, $a/\sqrt{2}$ is the distance between two lines in the 45° and 135° directions.

Pore and fracture areas are approximated by counting the number of pixels in object X:

$$A(x)=\int_{R^2}\mathrm{d}x\mathrm{d}y=\sum_{i,j}g\left(x_i,x_j\right) \tag{3}$$

In two-dimensional analysis, the equivalent diameter (EqD) is defined as the diameter of a disk with the same area, as indicated in Eq. (4):

$$\mathrm{Eq}D=\sqrt{\frac{4A}{\pi}} \tag{4}$$

Furthermore, fractal theory is applied to assess the complexity of pore morphology. If the pores display fractal characteristics, their areas and perimeters are mathematically expressed as:

$$\lg L=\frac{D_1}{2}\lg A+C_\mathrm{P} \tag{5}$$

where L denotes the perimeter measured in nanometers, A represents the pore area, D_1 is the fractal dimension describing pore morphology, and C_P is a constant.

3. Results

3.1. Distribution characteristics of shale components

Precise component identification of shale is a core aspect of shale research and forms the basis for characterizing organic and inorganic pore structures. Fig. 2 presents the precise multiphase component identification and the quantitative statistical results derived from backscattered SEM images. The shale skeleton primarily consists of brittle minerals, such as calcite (red) and quartz (blue), which exhibit poor to moderate grain roundness and angular to sub-angular geometry (Fig. 3(a1)–(a3), (a7)–(a9)). Notably, quartz and feldspar are loosely arranged and often form irregular grain contacts with calcite (Fig. 3(a2)). The primary calcareous mineral grains are moderately rounded, poorly sorted, and feature numerous dissolved voids and fractures (Fig. 3(a1)–(a8)), while secondary calcite crystals are more

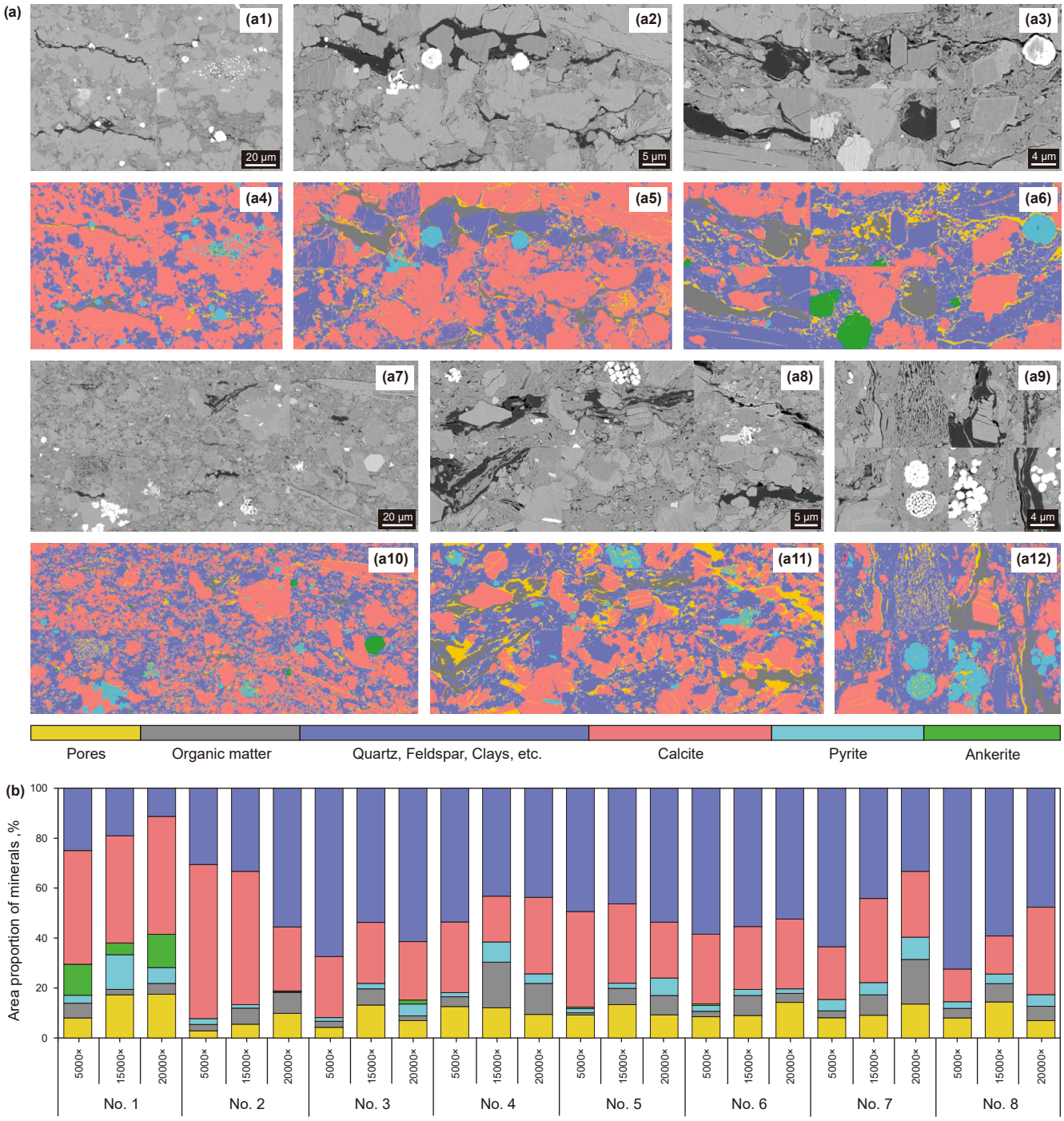

Fig. 3. Backscatter scanning electron microscopy images (SEM–BSE) and mineral component identification results (**a**) and statistical results of the proportion of major minerals (**b**). In Fig. (a), sub-images (**a1**)–(**a3**) and (**a7**)–(**a9**) show the spliced SEM–BSE images of No. 2 and No. 5 at magnifications of 5000×, 15000×, and 20000×, respectively. Sub-images (**a4**)–(**a6**), and (**a10**)–(**a12**) show the corresponding shale group segmentation results.

euhedral, exhibit rhombohedral morphology, and display minimal intergranular porosity (Fig. 3(a8)). Additionally, the clay mineral assemblage mainly comprises illite-montmorillonite mixed layers and illite. The illite layer fills gaps between brittle minerals, forming honeycomb, mesh, and cotton-like structures with well-developed intercrystalline pores (Fig. 3(a11)). Illite appears filamentous and feathery, often adhering to particle surfaces, and its aggregates form bridging structures, leading to heterogeneity in intercrystalline pore morphology (Fig. 3(a3)).

Segmentation and identification of the shale components and pores, along with the quantitative statistical results, are essential for further characterization of organic and inorganic pore structures (Fig. 3(b) and Table 2). The total pore area ranges from 2.81% to 17.5%, with an average of 10.0%. The degree of pore development varies, reflecting the rapid vertical changes in the lacustrine sediments of the Shahejie Formation. The organic matter area spans 0.96%–18.2%, with an average of 6.21%, indicating a heterogeneous distribution. Inorganic minerals occupy 68.5%–94.6% of the total

Table 2
Results of multiphase mineral identification under different magnifications of SEM images.

Sample No.	5000×, %					15000×, %					20000×, %				
	PV	OM	Py	Cal	Qz, Cl, etc.	PV	OM	Py	Cal	Qz, Cl, etc.	PV	OM	Py	Cal	Qz, Cl, etc.
1	7.87	5.86	3.15	44.86	24.61	17.19	2.16	13.94	42.85	19.00	17.48	4.39	6.33	4.72	51.01
2	2.81	2.62	2.34	61.72	30.50	5.47	6.28	1.45	52.69	32.84	9.47	8.12	0.18	24.76	53.54
3	4.19	2.42	1.49	24.41	67.17	13.10	6.54	2.09	24.43	53.51	6.87	1.94	4.81	23.39	61.41
4	12.61	3.90	1.65	28.29	53.48	12.04	18.20	8.11	18.32	43.11	9.40	12.47	3.77	30.60	43.72
5	8.96	0.96	1.64	37.55	48.49	13.30	6.51	2.13	31.79	46.25	9.14	7.73	6.90	22.14	53.16
6	8.51	2.16	2.28	27.84	58.38	8.97	8.05	2.43	25.17	55.32	14.27	3.54	1.82	27.97	52.37
7	8.02	2.74	4.61	21.02	63.27	9.08	8.11	4.90	33.57	44.02	13.62	17.83	8.90	26.38	33.24
8	7.25	3.49	2.37	11.92	65.55	14.39	7.30	3.80	15.19	58.98	6.89	5.78	4.65	34.99	47.53

PV: Pore volume; OM: Organic matter; Py: Pyrite; Cal: Calcite; Qz: Quartz; Cl: Clays.

area, averaging 82.8%. Among these, quartz and clay minerals comprise the largest share, ranging from 19.0% to 67.2%, with an average of 48.4%, highlighting their dominant role in the shale reservoir. Calcite and other calcium minerals follow, contributing 11.9%–61.7%, averaging 30.8%. Pyrite, in contrast, occupies a smaller share, ranging from 0.18% to 13.9%, with an average of 3.99%.

3.2. Pore types

The shale of the Shahejie Formation in the Dongying Sag is a typical mixed fine-grained sedimentary rock with relatively complex sedimentary components, which leads to the diversity and complexity of the types of pore networks in the shale. Previous researchers divided the pores into organic and inorganic pores based on their size and spatial correlation with minerals. Inorganic pores are divided into intergranular pores, intragranular pores, and fractures (Loucks et al., 2012). This paper summarizes the pore types and morphologies developed in shales.

Intragranular pores include pyrite intragranular pores, calcite and dolomite dissolution intragranular pores, and clay mineral intragranular pores (Fig. 4(a)–(d)). The pores in pyrite grains are located between pyrite crystals, forming strawberry-shaped or irregular aggregates with pore sizes ranging from tens to hundreds of nanometers (Fig. 4(a)). Dissolution pores of carbonate minerals (dolomite, calcite) are mostly found at particle boundaries or

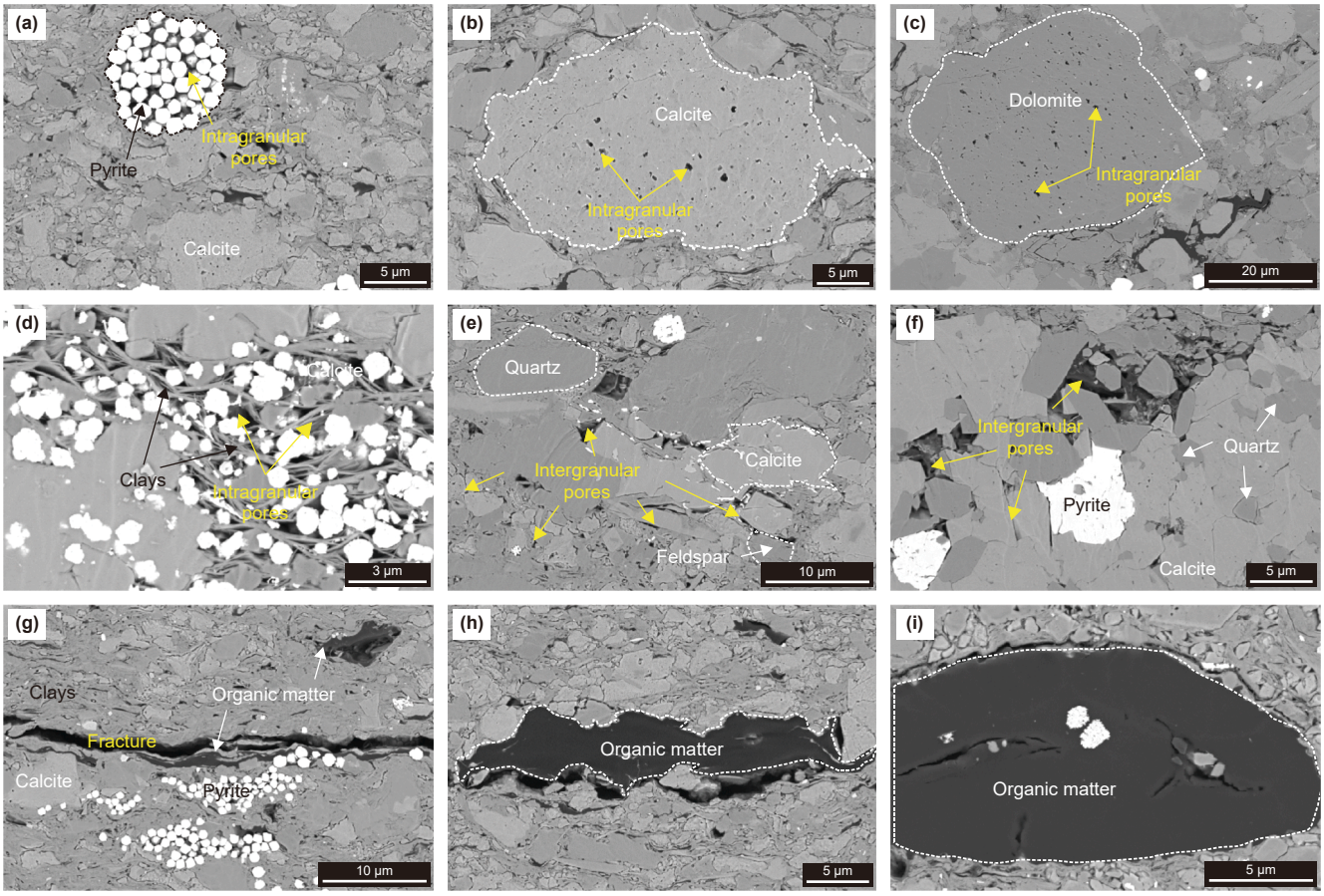

Fig. 4. Typical pore types of shale samples. (**a**) Intragranular pores within pyrite aggregates; (**b**) intragranular dissolution pores of calcite; (**c**) intragranular dissolution pores of dolomite; (**d**) intragranular pores within clay mineral aggregates; (**e**) intergranular pores existing between particles of brittle minerals (quartz, feldspar, carbonate minerals, etc.); (f) micro-fractures within the shale; (**g**)–(**i**) pore types associated with organic matter.

crystal surfaces. These pores are irregular in shape, mainly circular and polygonal, with diameters ranging from a few nanometers to hundreds of nanometers (Fig. 4(b) and (c)). Clay mineral intercrystalline pores are a common type of intergranular pores in shale reservoirs, which directly impact the specific surface area and micropore abundance (<1 μm) of shale. They usually appear in flaky, layered, and irregular forms between clay mineral particles or layers. The pore size is usually between a few nanometers and tens of nanometers (Fig. 4(d)). Although the tiny size and low connectivity of clay mineral intercrystalline pores limit the permeability of the reservoir, they are still an important space for oil and gas storage and migration, and have a direct impact on the mobility, permeability, and recoverability of shale oil and gas.

Intergranular pores are the primary place for oil and gas storage and migration in shale reservoirs and directly affect the effective porosity and permeability of the reservoir. They are mainly composed of incompletely filled pores between particles of brittle minerals (e.g., quartz, feldspar, calcite, etc.). They are usually slit-shaped, wedge-shaped, or irregular, with pore sizes ranging from nanometers to micrometers, with micrometer-sized pores being the main ones, providing larger storage space. The particle sorting, stacking mode, and diagenesis during the sedimentation process affect the size and distribution of intergranular pores. In particular, compaction and cementation during diagenesis may lead to a reduction in porosity (Milliken and Curtis, 2016).

Fractures are key channels for shale oil migration, and their formation and development are significantly affected by sedimentation and diagenesis (Hu, 2022). Some fractures may be artificial fractures produced during sample processing. However, to a certain extent, they can still reflect the potential fracture development characteristics of the reservoir under in-situ fracturing conditions. These fractures are usually distributed in a network, ranging in size from micro-fractures (<1 μm) to small fractures (1–10 μm), and mainly extend along the boundaries of brittle minerals (such as calcite, quartz) or expand in clay minerals and organic matter. Local fractures can even extend to several millimeters. Some fractures are filled with organic matter or minerals (such as calcite), indicating the influence of diagenetic fluid activity on fracture preservation and evolution (Fig. 4(f)). The network characteristics of fractures and their connectivity with other pores significantly enhance the permeability of the reservoir and build efficient oil and gas migration channels.

The shale of Shahejie Formation in the Dongying Sag is at a low-middle maturity stage and is in the early and middle oil generation period. The organic matter is amorphous under the SEM, and foam-like pores similar to those in high-mature shales are rare. Instead, it is dominated by organic-inorganic interface pores, which are located at the boundaries between organic matter and adjacent mineral phases (such as quartz, feldspar and clay minerals) (Fig. 4(g)–(i)). These pores are usually slender or irregularly shaped slits, parallel to the bedding or mineral grain boundaries. These pores are usually slender or irregularly shaped slits, parallel to the bedding or mineral grain boundaries, and their widths are usually hundreds of nanometers to several microns (Fig. 4(h)). A small number of wedge-shaped or slit-shaped shrinkage pores can be observed inside some organic matter, with a width of usually hundreds of nanometers (Fig. 4(i)). They are usually surrounded by amorphous organic matter and have poor connectivity.

3.3. Surface porosity

Surface porosity is an important indicator for quantitatively characterizing shale reservoirs' pore development degree and structural characteristics. It is a key parameter for reservoir evaluation and resource potential prediction (Wang and Zhang, 2019). Fig. 5(a) shows the distribution of shale organic-inorganic surface porosity at different magnifications, with an overall range of 2.81%–17.5% and an average of 10.0%; at low magnification (5000×), the surface porosity range is 2.81%–12.6%, with an average of 7.53%. At medium magnification, the surface porosity ranges from 5.47% to 17.2%, with an average of 11.7%, and at high magnification, the surface porosity ranges from 6.87% to 17.5%, with an average of 10.9%. The porosity of the sample surface shows nonlinear changes at different magnifications. The porosity of samples 1, 2, 6, and 7 increases continuously with magnification; the porosity of samples 3, 5, and 8 increases first and then decreases, and the porosity of sample 4 decreases constantly.

The exploration potential and development efficiency of shale oil are significantly affected by the characteristics of organic and inorganic pore networks, which determine the reserves of shale oil and its release and migration. Fig. 5(b) shows the proportion of organic-inorganic pores in the total pores. The surface porosity of organic matter ranges from 4.37% to 31.6%, with an average of 14.9%. In contrast, the contribution of inorganic porosity to pore volume ranges from 68.4% to 95.6%, with an average of 85.1%. Among them, quartz and clay minerals make the most significant contribution to inorganic porosity, with proportions ranging from 29.2% to 72.3%, with an average of 49.8%. This is followed by calcite-related pores, whose proportion ranges from 6.18% to 40.1%, with an average of 23.7%. Other significant contributing inorganic minerals include pyrite (9.65%) and unclassified minerals (6.72%)

3.4. Pore size distribution

Pore size distribution (PSD) is an important parameter for evaluating the connectivity and storage properties of shale reservoirs and is of great significance for revealing the storage capacity and fluid migration characteristics of the reservoir (Xia et al., 2021; Qian et al., 2022). Fig. 6 shows the PSD of extracted pores from SEM images of three typical samples. The pore diameters are mainly 20 nm to 10 μm, and the central peak PSD distribution is 200–1000 nm. It is worth noting that significant differences in the PSD of the central peak were observed at different magnifications for the same sample; specifically, as the magnification increases, the central peak PSD shifts from smaller pores to larger pores, mainly because high magnification makes it easier to capture nanoscale pores. In comparison, low magnification tends to highlight the contribution of larger pores, reflecting the heterogeneity of the sample in the multi-scale pore structure to a certain extent.

Nanopores provide the primary source of the total pores in different scale ranges. The total number of pores in all shale observation fields ranges from 2386 to 39671, with an average of 13126. It is worth noting that 99.1% of the pores have a diameter of less than 1000 nm, that is, nanopores. Among them, the number of small pores (<200 nm) ranges from 2090 to 29400, with an average of 10225, accounting for 60.5%–95.4% of the total pores, with an average of 80.6%. With the increase of magnification and the decrease of field area, the total number of pores also decreases accordingly, and the proportion of small pores increases further. At a magnification of 5000 times, the average number of pores is 21736, of which small pores (<200 nm) account for an average of 68.9%. At a magnification of 15000× , the number of pores was reduced to 10772, with small pores accounting for an average of 84.5%. At a magnification of 20000 times, the total number of pores was only 6870, with small pores accounting for an average of 88.3% (Table 3).

Although nano-scale pores account for an absolute majority of the total pore volume in shale, the pore space they provide is

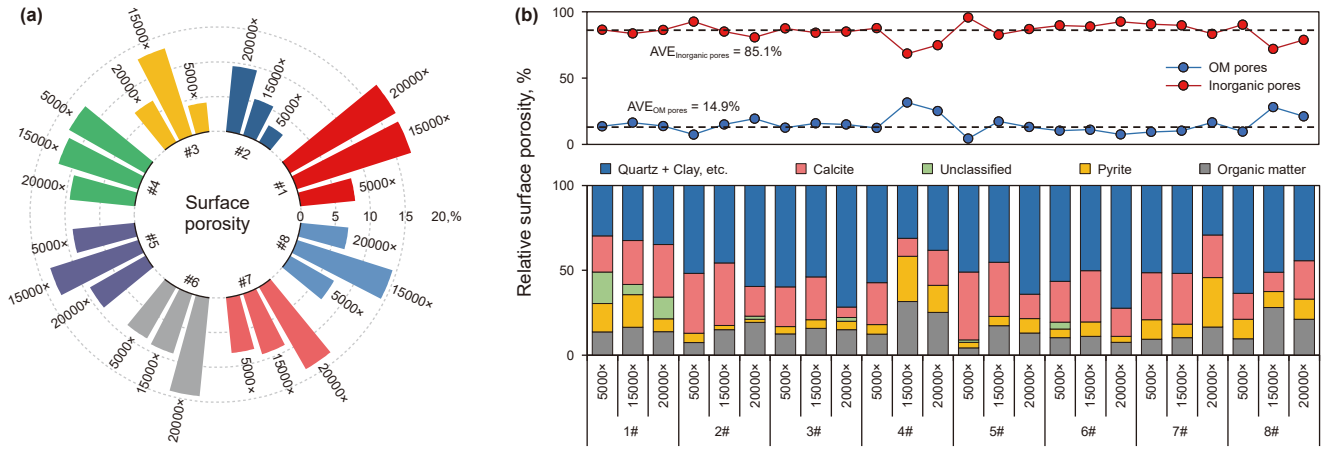

Fig. 5. Results of surface porosity at 5000×, 15000×, and 20000× magnifications of SEM images. (**a**) The total surface porosity, and (**b**) the surface porosity results of organic-inorganic pores.

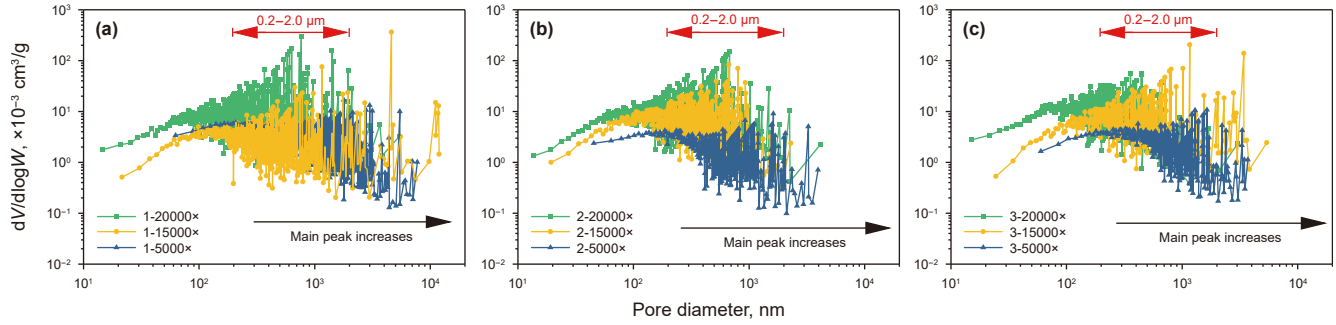

Fig. 6. Pore size distribution characteristics of total surface pores for Samples Nos. 1–3. (**a**)–(**c**) at different magnifications (5000×, 15000×, and 20000×) of SEM images.

Table 3
Counting results of total pores, organic and inorganic pores.

Magnification	Pore size, nm	Counts				
		Total pores	Cal pores	OM pores	Pyrite pores	Q-Cl pores
5000×	Full-scale	9448[a]–39671[b] (21736[c])	2055[a]–16196[b] (7673[c])	509–8087 (1845)	101–7120 (1715)	7572–24968 (15425)
	0–200	6103–29400 (15,162)	1026–10947 (4802)	303–4931 (1121)	76–3645 (908)	4634–16363 (10129)
	0–1000	9114–39043 (21,441)	1993–15901 (7481)	472–7997 (1768)	100–6886 (1639)	7340–24590 (15149)
	>1000	75–628 (295)	39–468 (192)	12–190 (77)	1–234 (76)	75–557 (277)
15000×	Full-scale	2852–23586 (10,773)	757–5852 (2858)	272–2289 (1006)	101–2836 (1115)	1416–15892 (6290)
	0–200	2185–21847 (9376)	524–4737 (2259)	177–2004 (790)	66–2456 (881)	991–14452 (5288)
	0–1000	2809–23505 (10,715)	732–5837 (2829)	250–2261 (984)	96–2789 (1098)	1349–15845 (6251)
	>1000	17–88 (58)	15–73 (29)	6–49 (22)	1–47 (17)	15–67 (39)
20000×	Full-scale	2386–12765 (6871)	237–3391 (1136)	210–3831 (996)	63–3831 (1311)	1596–6633 (4542)
	0–200	2090–12182 (6139)	212–2632 (878)	187–3744 (865)	49–3744 (1153)	1366–5662 (3943)
	0–1000	2369–12748 (6843)	236–3342 (1123)	207–3823 (984)	62–3823 (1301)	1583–6583 (4520)
	>1000	5–50 (28)	1–49 (13)	3–25 (13)	1–47 (10)	7–50 (22)

Variables a, b, and c denote the minimum, maximum, and average values. These statistical measures describe the range and central tendency of the dataset under investigation.

comparable to that of micro-scale pores, with an absolute surface porosity ranging from 1.86% to 7.23%, with an average of 5.06%. It accounts for about 55.2% of the total surface porosity. Among them, the absolute surface porosity provided by pores <200 nm is only 0.43%–2.08%, with an average of 1.14%, accounting for 12.7% of the total surface porosity (Table 3). The pore space provided by micro-scale pores accounts for about 44.8% of the total surface porosity. The contribution of a single micro-scale pore to the surface porosity (number of pores/corresponding surface porosity) is about 160 times that of nano-scale pores.

The pore size distribution (PSD) of organic and inorganic pores of all samples was characterized. In the shale samples of this study, the PSD of organic and inorganic pores is generally consistent and unimodal. Therefore, taking sample 2 as a representative, Fig. 7 shows that the PSD of various pore types such as organic matter, calcite, pyrite and quartz-clay is in the range of 10 nm to 4 μm, and most of the pores are concentrated between 200 nm and 1 μm.

The PSD distribution of organic pores is relatively wide (40 nm to 3 μm at 5000 times magnification; 20 nm to 2 μm at higher magnification), with the main peak around 700–800 nm

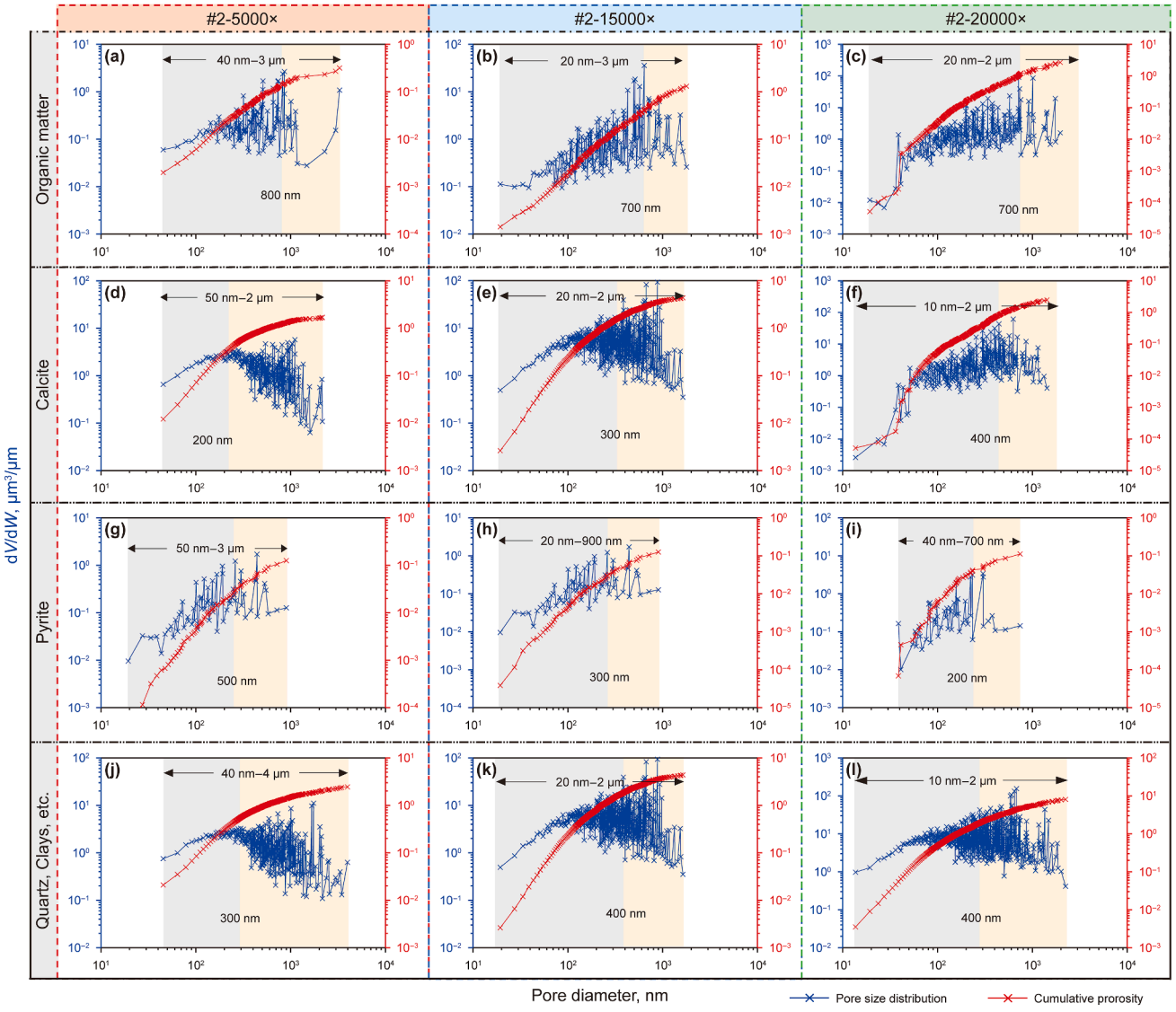

Fig. 7. PSD of major minerals for Sample No. 2 at different magnifications of SEM images.

(Fig. 7(a)–(c)). Although the organic pores are widely distributed, their proportion is relatively low, accounting for only 2.18%–26.7% of the total pores, with an average of 8.29%. This shows that compared with other mineral-dominated pore types, there are fewer pores in organic matter, but the pores are larger. Calcite-dominated pores also show a wide distribution range (50 nm–3 μm), but the average pore size is smaller (with a main peak around 200–300 nm), and the pore network is more developed than that of organic matter (Fig. 7(d)–(f)). Pyrite-dominated pores range in size from 20 nm to 900 nm, typically peaking around 300–500 nm, showing a moderate porosity contribution (Fig. 7(g)–(i)). Quartz, clays, and other silicates have the widest range of pore sizes (10 nm–4 μm) with a relatively uniform distribution, but a peak around 300–400 nm (Fig. 7(j)–(l)).

In addition, the cumulative surface porosity curve (red line in the figure) shows that organic matter and pyrite contribute less to the total surface porosity, while calcite and silicate-dominated pores provide higher cumulative porosity, especially in the moderate size range (200–800 nm). Higher magnification images (No. 2-15000× and No. 2-20000×) improve the peak distribution resolution and confirm the effective pore volume in the 200–800 nm range, especially the contribution of inorganic components. Despite the larger size of organic pores, their limited abundance reduces their contribution to the total porosity. In contrast, in the medium-to low-maturity lacustrine shale samples studied, calcite and quartz-clay related pores contribute more to the total pore volume and connectivity due to their more developed and more evenly distributed networks.

The number of organic and inorganic pores is shown in Table 4. The number of organic-inorganic pores is consistent with the distribution trend of total pores, both of which are exponentially distributed. Among all the organic-inorganic pores of the samples, inorganic mineral pores are dominant, among which quartz and clay minerals have the most significant number of pores, with an average of 8752, accounting for 58.1% of the total number of pores, and an absolute porosity of 7.66%, accounting for 48.2% of the total porosity. Nanoscale pores are dominant, accounting for 98.7% of the total pores and 57.3% of the surface porosity of quartz and clay pores. Pores with a pore size of less than 200 nm account for 76.6% of the quartz and clay pores and only contribute 12.0% of the surface porosity. On the contrary, although pores larger than 1 μm account for a relatively small proportion (the number of pores

Table 4
Statistical results of surface porosity of total pores, organic and inorganic pores.

Magnification	Pore size, nm	Surface porosity, %				
		Total pores	Calcite	Organic matter	Pyrite	Quartz, clays, etc.
5000×	Full-scale	2.81[a]–12.61[b] (7.53[c])	1.35–8.64 (3.98)	0.73–5.12 (1.84)	0.16–6.72 (1.84)	2.81–12.54 (6.86)
	0–200	0.43–1.02 (0.65)	0.15–0.86 (0.42)	0.02–0.19 (0.1)	0.02–0.39 (0.13)	0.12–1.4 (0.83)
	0–1000	1.86–6.74 (3.93)	0.83–3.91 (1.78)	0.16–1.39 (0.52)	0.13–1.55 (0.5)	1.86–5.29 (3.36)
	>1000	0.95–8.52 (3.59)	0.32–7.09 (2.2)	0.42–4.61 (1.32)	0.04–6.08 (1.34)	0.95–8.87 (3.5)
15000×	Full-scale	5.47–17.19 (11.69)	1.83–7.47 (4.73)	1.02–6.19 (3.62)	0.16–5.48 (2.28)	4.47–12.77 (7.82)
	0–200	0.56–2.08 (1.3)	0.15–0.86 (0.42)	0.02–0.19 (0.1)	0.02–0.39 (0.13)	0.12–1.4 (0.83)
	0–1000	2.23–7.29 (5.33)	1.12–3.78 (2.34)	0.2–2.37 (0.98)	0.13–2.22 (0.8)	0.95–4.81 (3.89)
	>1000	0.9–14.96 (6.36)	0.44–6.02 (2.39)	0.42–5.11 (2.65)	0.04–4.67 (1.47)	0.69–8.6 (3.93)
20000×	Full-scale	6.87–17.48 (10.89)	0.71–11.34 (3.31)	1.28–9.3 (3.49)	0.18–9.3 (2.47)	0.18–9.82 (2.47)
	0–200	1.13–1.91 (1.47)	0.09–0.71 (0.3)	0.05–0.28 (0.14)	0.03–0.48 (0.26)	0.74–1.73 (1.19)
	0–1000	4.08–7.10 (5.9)	0.36–4.5 (1.87)	0.41–1.82 (1.06)	0.11–3.13 (1.25)	2.9–6.03 (4.82)
	>1000	1.45–10.64 (4.99)	0.16–6.84 (1.44)	0.55–8.07 (2.43)	0.07–6.68 (1.22)	0.68–9.32 (3.47)

Variables a, b, and c denote the minimum, maximum, and average values.

ranges from 7 to 557, with an average of 113), they contribute approximately 42.7% of the porosity.

Among inorganic mineral pores, calcite ranks second in terms of pore abundance, with pore numbers ranging from 237 to 16196 (average 3889), accounting for 23.0% of the total pore number, and the average absolute porosity is 4.01%. The average number of pores <200 nm, <1 μm, and >1 μm are 2646, 3811, and 78, respectively, accounting for 71.8%, 98.2%, and 1.84% of the calcite-related pore number and contributing to the calcite surface porosity by 9.37%, 58.5%, and 41.7%, respectively.

The number of organic pores is relatively small, ranging from 210 to 8087 (average 1282), which accounts for 8.55% of the total pore number. This corresponds to an absolute porosity of 2.98%, representing 17.28% of the total porosity. Nanopores account for about 95.3% of the number of organic pores (1376) and 33.0% of the organic surface porosity (absolute porosity 0.75%), of which 925 are <200 nm, accounting for 72.0% of the number of organic pores and 3.95% of the organic porosity. Although micron-sized pores only account for 3.83% of organic pores, they contribute 65.3% of the organic surface porosity.

It is worth noting that regardless of organic-inorganic pores, micron-sized pores are the main contributors to the pore space, and their surface porosity accounts for 50% of the total porosity. In addition, although the number of organic pores is much less than that of inorganic pores, the average pore size of a single pore of organic pores, which is mainly large, is significantly larger than that of inorganic pores, and the surface porosity they provide is about 2.2–2.6 times that of inorganic minerals.

3.5. Pore fractal characteristics

The fractal dimension (D_1) is a quantitative indicator of the complexity of the pore morphology. The larger its value, the more complex the pore morphology and the higher the surface roughness (Wang et al., 2004; Zhang et al., 2023). Generally, the fractal dimension is calculated by analyzing the double logarithmic relationship between the pore area and the perimeter, and the specific calculation formula is shown in Eq. (5). The pore area and the perimeter have typical fractal characteristics, and the data points show a good linear correlation in the log-log coordinate diagram (Fig. 8).

The fractal dimension of total pores showed a gradually decreasing trend with increased magnification. At a magnification of 5000×, the fractal dimension ranged from 1.813 to 1.921, with an average value of 1.872; at a magnification of 15000×, the fractal dimension ranged from 1.645 to 1.865, with an average value of 1.765; and at a magnification of 20000×, the fractal dimension further decreased, ranging from 1.572 to 1.799, with an average value of 1.717 (Table 5). The fractal dimension of organic-inorganic pores also showed a similar trend. At a magnification of 5000×, the fractal dimensions of organic pores, calcite pores, and quartz-clay pores were 1.807, 1.849, and 1.852, respectively; when the magnification increased to 20000 times, the fractal dimensions decreased to 1.636, 1.665, and 1.689, respectively. A comparison of organic-inorganic pores shows that the fractal dimension of calcite pores, which have the most significant number of pores, is similar to that of quartz and clay pores, showing high structural complexity and strong fractal characteristics. In contrast, the fractal dimension of organic pores, mainly organic-inorganic interface pores, is generally low, and the structural complexity and heterogeneity are relatively weak.

4. Discussion

4.1. Effect of different magnifications of SEM on surface porosity

Significant differences exist in evaluating the number of shale pores and surface porosity from SEM images at different magnifications. In particular, the ability to identify micro-pores increases significantly with the increase in magnification. By normalizing the number of pores per square micron and surface porosity calculations, the statistical bias introduced by changes in the field of view is alleviated, allowing the pore development characteristics at different scales to be more accurately characterized (Fig. 9). This analysis method provides a supplement and improvement over previous studies that only used fixed magnification or single-scale observation.

Compared with previous studies, this result further deepens the understanding of the relationship between representative equivalent volume (REV) and pore development characteristics. In traditional research, the selection of REV is usually based on the uniformity of rock components and the consistency of pore distribution, while less attention is paid to the impact of different magnifications and scale changes on REV volume evaluation. For example, Zhang et al. (2023) found through a multi-viewpoint observation method that a larger REV volume helps capture the overall distribution characteristics of the pore network but may underestimate the contribution of microscale pores, while Arif et al. (2021) emphasized that at the microscale Under this condition, SEM images from a single field of view may not fully characterize the heterogeneity of pores. Our study shows that as the SEM magnification increases from 5000× to 20000×, the number of small pores (0–200 nm) increases significantly (about 5.48 times), while the number of mesopores (200–1000 nm) and

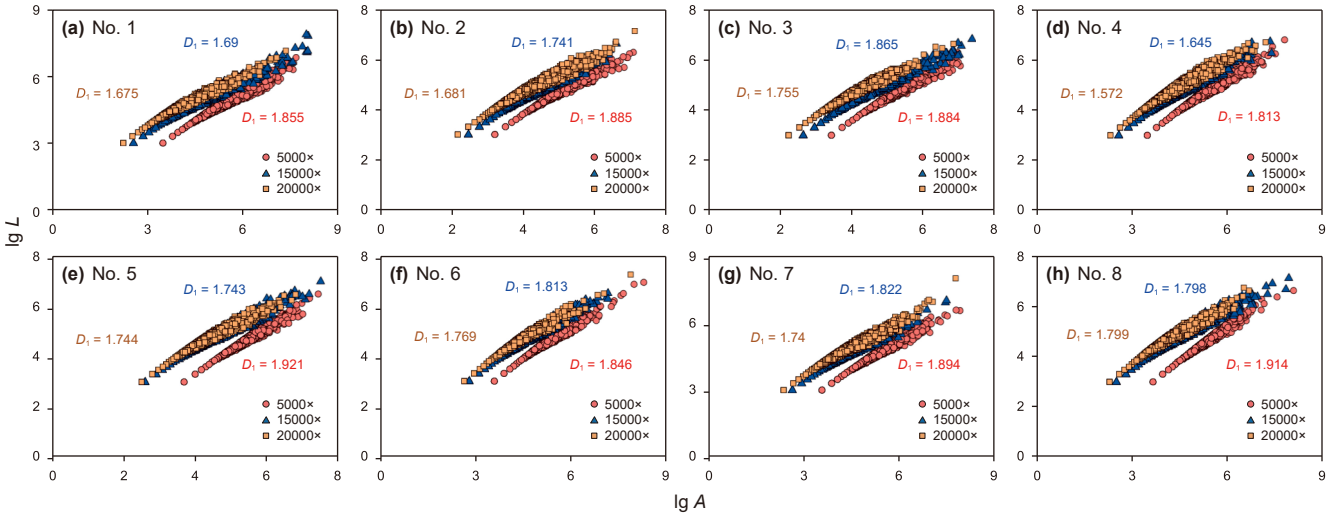

Fig. 8. Fractal characteristics of total pores for shale samples at different magnifications.

Table 5
Results of fractal dimension for different pore types.

Magnification	Pore type	Sample No.							
		1	2	3	4	5	6	7	8
5000×	Total pore	1.8552	1.8852	1.8438	1.8128	1.9208	1.8456	1.8944	1.9140
	OM pore	1.8294	1.7812	1.7814	1.7598	1.8686	1.7608	1.8461	1.8322
	Cal pore	1.8414	1.8534	1.8594	1.7742	1.8922	1.8142	1.8628	1.8956
	Q-Cl pores	1.8344	1.8372	1.8388	1.7968	1.8922	1.8318	1.8822	1.8994
	Pyrite pores	1.8386	1.6904	1.8636	1.7448	1.8632	1.8314	1.8548	1.8403
15000×	Total pore	1.6931	1.7404	1.8652	1.6448	1.7432	1.8128	1.8224	1.7984
	OM pores	1.5364	1.6909	1.6374	1.5772	1.7044	1.7656	1.7740	1.6858
	Cal pores	1.6244	1.7064	1.6341	1.6328	1.7213	1.7842	1.8001	1.7542
	Q-Cl pores	1.5614	1.7064	1.6394	1.5908	1.7206	1.7918	1.8094	1.7919
	Pyrite pores	1.7082	1.6904	1.6524	1.6602	1.7014	1.7586	1.7816	1.7262
20000×	Total pore	1.6748	1.6812	1.7552	1.5724	1.7440	1.7692	1.7409	1.7988
	OM pores	1.6086	1.4281	1.6671	1.5066	1.6772	1.7372	1.6814	1.7780
	Cal pores	1.6054	1.5792	1.6976	1.5618	1.7532	1.7382	1.7032	1.6796
	Q-Cl pores	1.6576	1.6626	1.7251	1.5256	1.7260	1.7448	1.7236	1.7506
	Pyrite pores	1.7031	1.5308	1.6878	1.6114	1.6938	1.7924	1.7030	1.7782

Q-Cl pores: Quartz-Clays, etc. mineral pores; Cal pore: Calcite pores; OM pores: Organic matter pores.

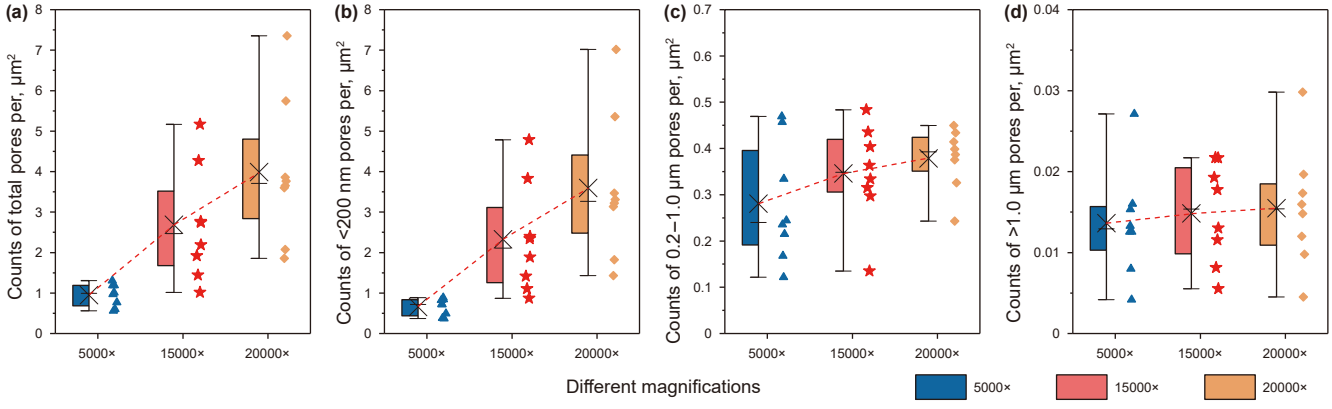

Fig. 9. Differences in the number of pores obtained from different magnifications of SEM images for eight samples.

macropores (>1 μm) changes relatively slowly (Fig. 9). This result shows that the pore distribution results obtained at different magnifications may correspond to different REV ranges, and the adequate identification of small pores requires higher magnification and smaller fields of view.

In addition, compared with the study by Hemes et al. (2013), which observed pore distribution at a fixed magnification (10000 times), this study revealed the nonlinear growth law of surface porosity as the magnification increases, especially for micro-pores. Recognition capabilities are significantly enhanced. This is highly

consistent with the pore development characteristics obtained by Gao et al. (2020) using multi-scale analysis. Still, this study further quantitatively analyzed the specific contributions of different pore size ranges (0–200 nm, 200–1000 nm, and >1 μm) under varying magnifications. For example, 0–200 nm small pores have the most significant increase in surface porosity (29.03 times), but due to the low initial porosity, their contribution to the total porosity is relatively limited, while the rise in 200–1000 nm mesopores mainly drives the total porosity growth (16.07 times), this finding confirms the dominant role of mesopores and macropores in reservoir capacity.

Moreover, these magnification-dependent observations mirror the diagenetic origins of the pores themselves. Early-diagenetic dissolution pores in calcite and dolomite tend to exceed 200 nm and are therefore only fully resolved at higher magnifications (Liang et al., 2024a, 2024b). In contrast, clay-mineral intercrystalline pores, generated during illite-smectite transformation under burial compaction, are finer (<200 nm) and can be detected at lower magnifications (Sun et al., 2018). This link between pore genesis and magnification response underscores the need to align REV selection not only with statistical uniformity but also with the geological scale of pore-forming processes.

The selection of REV volume is crucial in shale pore characterization. The results of this study show that as the magnification increases, the number of pores and surface porosity under different viewing fields show apparent differences. Zhao et al. (2023) proposed that the REV volume needs to balance microheterogeneity and overall homogeneity. The findings of this study support this view. They also pointed out that REV at a single scale may underestimate the contribution of pores in a specific pore size range to reservoir performance. This also shows that multi-scale analysis can capture the pore network characteristics more comprehensively by optimizing the field of view and magnification, thus providing a new basis for REV selection.

4.2. Influencing factors on pore networks

4.2.1. Mineral components

The structural properties of shale are the basis for the development of reservoir space, and the interaction between minerals and pore networks is an important factor affecting reservoir properties. However, the current understanding of the relationship between mineral types and their associated pore networks is mainly based on comparative analysis of different experimental results, and there is still uncertainty in the consistency of the results (Li et al., 2021; Xu et al., 2023). This study innovatively identified and segmented different minerals and their corresponding pore networks by quantitatively analyzing large-field SEM images. Fig. 10 shows the correlation between the area proportion of the main minerals and the related pores, showing a good linear correlation, expressed as $y = ax$. At a zero of minerals, the surface porosity is null. Upon doubling the area, the increment in surface porosity (denoted by the coefficient a) varies among minerals. The degree of development of related pores per unit area is explained by comparing the slopes.

Among the primary minerals in shale, the increase in pore volume per unit area of pyrite is as high as 2.53, which is closely related to the high specific surface area of pyrite intercrystalline pores. It is worth noting that pyrite is usually associated with organic matter in anoxic sedimentary environments, so it is easily

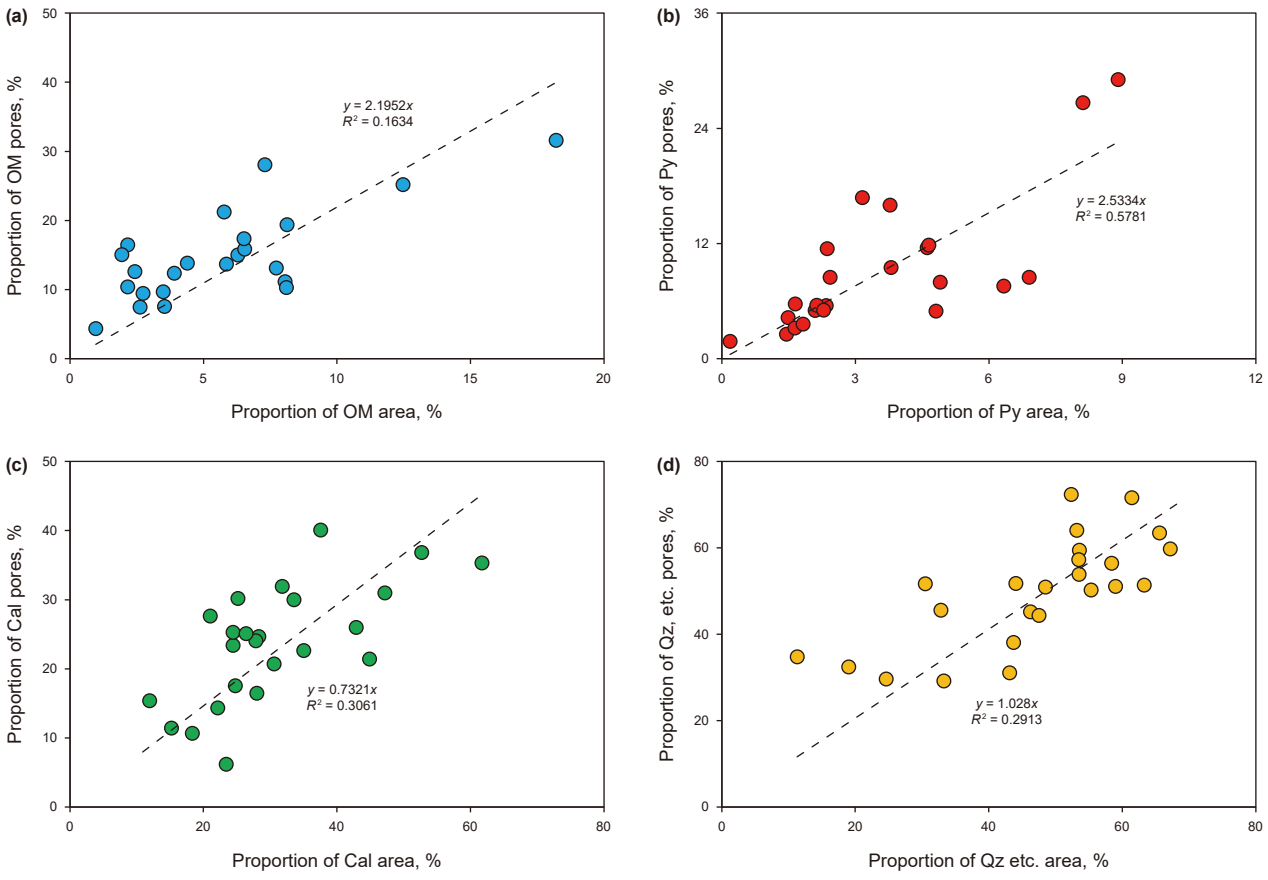

Fig. 10. Relationships between the area of different components and their surface porosity to varying magnifications. (**a**) Organic matter, (**b**) pyrite, (**c**) calcite (Cal), and (**d**) quartz.

affected by acidic fluids during diagenesis, forming abundant micron- and nano-scale pores locally. This heterogeneity will lead to spatial variability in the development of pore networks to a certain extent (Wilkin et al., 1996; Wilkin and Barnes, 1997). Furthermore, the surface porosity increment per unit area contributed by organic matter is 2.19, primarily associated with the extensive development of micropores and nanoscale pores formed during the early thermal cracking of kerogen. Because overall maturity remains low (T_{max} < 445 °C), organic pores are largely confined to organic-inorganic interfaces and intra-organic shrinkage pores, which are often isolated and poorly connected despite their high individual surface area (Chen and Xiao, 2014; Mathia et al., 2016). In contrast, the porosity increase driven by the increase in quartz and clay mineral content is relatively slow, with a surface porosity increment per unit area of 1.028. This is because minerals such as quartz rarely develop intragranular pores. In shale layers dominated by clay minerals, compaction causes the clay mineral-related pores to be gradually compacted, resulting in a low surface porosity increment per unit area (Milliken and Curtis, 2016; Sun et al., 2018). Calcite contributes the least to porosity development, with a unit-area surface porosity increment of only 0.732, This is because during the early diagenetic process of shale, organic acids (such as formic acid and acetic acid) produced by the decomposition of organic matter seep into the pores, forming a local acidic environment and causing the dissolution of dolomite or calcite (Liang et al., 2024a, 2024b), and early carbonate cementation can also occlude later-formed dissolution pores, further limiting its net contribution (Iqbal et al., 2021).

4.2.2. Pores of different sizes of organic and inorganic pores

The influence of different scales of pores of the main minerals in shale on the overall porosity of the reservoir is multifaceted and closely related to the diagenetic evolution process and the thermal evolution of organic matter. Fig. 11 shows the correlation analysis of different pore sizes (<200 nm, 0.2–1 μm, >1 μm) and minerals such as calcite, pyrite, organic matter, quartz, and clay.

As the pore size increases, its influence on the reservoir accommodation capacity gradually increases (Fig. 11). The correlation between pores smaller than 200 nm and the total porosity is low (the correlation coefficient is about 0.2), indicating that it contributes less to the effective reservoir space. This type of nanoscale pore is mainly controlled by the mineral structure characteristics and its compaction history (Loucks et al., 2009), and is often distributed in the interlayer and intercrystalline pores of clay minerals (Milliken and Curtis, 2016). In the early stage of diagenesis, these pores are often difficult to preserve due to high-pressure compaction and cement filling. However, its development degree is still related to the initial clay content, especially the presence of interlayer water inhibits the closure of pores to a certain extent.

Pores of 200 nm to 1 μm show a more significant positive correlation (correlation coefficient is about 0.6), indicating that they belong to the transitional pore system. This type of pore is mainly formed during the mid-diagenesis process, controlled by the dissolution of unstable minerals (such as feldspar and carbonate) by acidic fluids produced by pyrolysis of organic matter (Yang et al., 2020; Curtis et al., 2012). The correlation between this pore size and quartz and clay content can reach 0.76, further

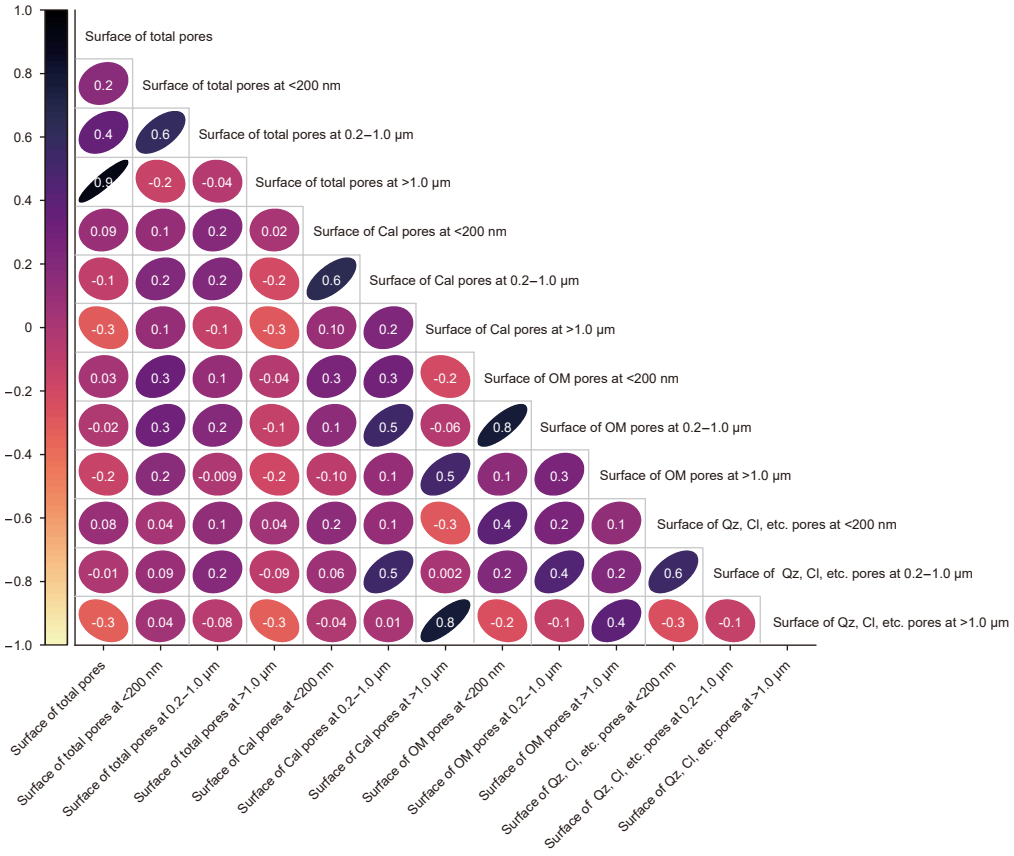

Fig. 11. Contribution of minerals-related pores at different pore size distributions to total porosity.

indicating that the formation of this type of pore is affected by both the compressive resistance of framework minerals such as quartz and the mineral phase transition of clay minerals such as montmorillonite to illite.

Pores larger than 1 μm have a very strong positive correlation with total porosity (correlation coefficient is about 0.9), indicating that macroscopic pores and fractures are the main sources of effective space in shale reservoirs. These pores are mostly formed in the late diagenesis and tectonic stress stage. Scanning electron microscopy analysis (Fig. 4(g)) reveals that micron-sized fractures are commonly developed between calcite and dolomite carbonate particles, reflecting the combined effects of mineral dissolution and brittle deformation (Sondergeld et al., 2010). Clay-rich layers are very prone to interlayer shear fracture under tectonic stress, forming micron-sized fractures, while organic-rich zones are prone to shrinkage fractures due to hydrocarbon degassing and volume shrinkage in the late thermal evolution (R_o >1.0%) (Guo et al., 2017). These fractures are closely related to fluctuations in temperature, pressure and water content (Wang and Zhang, 2019).

It can be seen that the formation mechanism of pores in shale is not only a function of mineral type, but also the result of the coupling of multiple geological processes such as diagenetic compaction, cementation, mineral transformation and thermal evolution of organic matter. Clay minerals mainly control the development of nanopores in the early diagenetic stage, while quartz and carbonates affect the expansion of fractures under the action of tectonic stress in the later stage. The thermal evolution of organic matter plays a key role in the secondary development of pores and the formation of micro-fractures (Curtis et al., 2012; Jarvie, 2012). In summary, the contribution of different mineral-related pores in the multi-scale pore structure reflects the complex geological evolution history. The nanopores controlled by clay minerals provide the basic framework, while the micron to millimeter-scale fractures are mainly controlled by the synergistic effect of multiple minerals, the evolution of organic matter and the heat-pressure changes caused by them, together forming a highly heterogeneous and interconnected pore networks, which is the key spatial basis for the storage and migration of shale oil and gas.

5. Conclusions

Based on high-resolution scanning electron microscope images of Shahejie Formation shales in the Dongying Sag, this study established a fast and reliable image segmentation method, accurately quantified pore and mineral distribution. It systematically revealed the microstructural characteristics and geological control factors of organic and inorganic pore networks in medium-to low-maturity lacustrine shales.

The study identified three main types of pores: (1) nanoscale intragranular pores, including pores within pyrite crystals, calcite and dolomite dissolution pores, and clay mineral intergranular pores; (2) nanometer to micrometer-scale intergranular pores, such as pores between mineral particles and organic-inorganic interface pores; (3) micron to millimeter-scale microcracks, mainly distributed at the interlayer interface between clay and carbonate minerals. Quantitative analysis shows that inorganic pores are about ten times more numerous than organic pores, contributing more than 85% of the surface porosity, and have a more complex overall morphology; while organic pores, although fewer in number, have a larger average pore size and contribute a higher pore volume to each pore, about 2.2–2.6 times that of inorganic pores, and contribute about 15% to the overall reservoir.

The pore networks of shale are mainly controlled by the micron-scale pores, especially the structure composed of interlayer fractures between clay minerals and calcite. Furthermore, the inorganic pores related to clay minerals constitute the nanoscale reservoir space. Organic pores also contribute to the submicron pore scales. These insights provide a foundation for optimizing medium-to low-maturity shale oil exploration strategies, especially in early resource assessment.

However, the conclusions of this study are based on single-well, single-layer formation samples, which may limit their wider applicability. Future studies will expand the spatial coverage to cover different sedimentary facies and maturity settings, and combine advanced imaging techniques with geological backgrounds to further explore the control of mineral assemblages and diagenetic pathways on the evolution of pore systems.

CRediT authorship contribution statement

Zi-Zhi Lin: Writing – original draft, Software, Methodology, Conceptualization. **Qin-Hong Hu:** Writing – review & editing, Funding acquisition. **Na Yin:** Writing – review & editing, Data curation. **Yu-Shan Du:** Supervision, Resources. **Jing Chao:** Supervision, Resources. **Guang-Lei Zhang:** Supervision. **Song-Tao Wu:** Supervision.

Declaration of competing interest

The authors declare that they have no known competing financial interests or personal relationships that could have appeared to influence the work reported in this paper.

Acknowledgments

This work was financially supported by a Provincial Major Type Grant for Research and Development from the Department of Science & Technology of Shandong Province (Grant No. 2020ZLYS08), an Innovation fund project for graduate student of China University of Petroleum (East China), and the Fundamental Research Funds for the Central Universities (25CX04016A).

References

Aili, A., Maruyama, I., 2020. Review of several experimental methods for characterization of Micro- and nano-scale pores in cement-based material. Int. J. Concrete Struct. M. 14 (1), 55. https://doi.org/10.1186/s40069-020-00431-y.

Arif, M., Mahmoud, M., Zhang, Y.H., Iglauer, S., 2021. X-ray tomography imaging of shale microstructures: A review in the context of multiscale correlative imaging. Int. J. Coal Geol. 233, 103641. https://doi.org/10.1016/j.coal.2020.103641.

Behar, F., Beaumont, V., Penteado, H.L., Lewan, M., 2001. Rock-Eval 6 technology: Performances and developments. Oil Gas Sci. Technol. 56 (2), 111–134. https://doi.org/10.2516/ogst:2001013.

Chalmers, G.R., Bustin, R.M., 2008. Lower Cretaceous gas shales in northeastern British Columbia, part I: Geological controls on methane sorption capacity. Bull. Can. Petrol. Geol. 56 (1), 1–21. https://doi.org/10.2113/gscpgbull.56.1.1.

Chen, J., Xiao, X.M., 2014. Evolution of nanoporosity in organic-rich shales during thermal maturation. Fuel 129, 173–181. https://doi.org/10.1016/j.fuel.2014.03.058.

Curtis, M.E., Sondergeld, C.H., Ambrose, R.J., Rai, C.S., 2012. Microstructural investigation of gas shales in two and three dimensions using nanometer-scale resolution imaging. AAPG Bull. 96 (4), 665–677. https://doi.org/10.1306/08151110188.

Gao, Z.Y., Fan, Y.P., Xuan, Q.L., Zheng, G.W., 2020. A review of shale pore structure evolution characteristics with increasing thermal maturities. Adv. Geo-Energy Res. 4 (3), 247–259. https://doi.org/10.46690/ager.2020.03.03.

Guo, H.J., Jia, W.L., Peng, P.A., Zeng, J., He, R.L., 2017. Evolution of organic matter and nanometer-scale pores in an artificially matured shale undergoing two distinct types of pyrolysis: A study of the Yanchang shale with type II kerogen. Org. Geochem. 105, 56–66. https://doi.org/10.1016/j.orggeochem.2017.01.004.

Hemes, S., Desbois, G., Urai, J.L., De Craen, M., Honty, M., 2013. Variations in the morphology of porosity in the boom clay formation: Insights from 2D high-resolution BIB-SEM imaging and mercury injection porosimetry. Neth. J. Geosci. 92, 275–300. https://doi.org/10.1017/S0016774600000214.

Hu, L., 2022. A review of mechanical mechanism and prediction of natural fracture in shale. Arabian J. Geosci. 15 (6), 474. https://doi.org/10.1007/s12517-022-09786-w.

Iqbal, O., Padmanabhan, E., Mandal, A., Dvorkin, J., 2021. Characterization of geochemical properties and factors controlling the pore structure development of shale gas reservoirs. J. Petrol. Sci. Eng. 206, 109001. https://doi.org/10.1016/j.petrol.2021.109001.

Jarvie, D.M., 2012. Shale resource systems for oil and gas: Part 2: Shale-oil resource systems. https://doi.org/10.1306/13321447M973489.

Li, X., Cai, J.G., Gao, B., Long, S.X., Feng, D.J., Peng, Z.Y., Guo, B.Q., 2021. Characteristics of shale pores and surfaces and their potential effects on the fluid flow from shale formation to fractures. Front. Earth Sci. 9, 751543. https://doi.org/10.3389/feart.2021.751543.

Li, W.B., Wang, J., Jia, C.Z., Lu, S.F., Li, J.Q., Zhang, P.F., Wei, Y.B., Song, Z.J., Chen, G.H., Zhou, N.W., 2024. Carbon isotope fractionation during methane transport through tight sedimentary rocks: Phenomena, mechanisms, characterization, and implications. Geosci. Front. 15, 101912. https://doi.org/10.1016/j.gsf.2024.101912.

Liang, C., Yang, B., Cao, Y.C., Liu, K.Y., Wu, J., Hao, F., Han, Y., Han, W.L., 2024a. Salinization mechanism of lakes and controls on organic matter enrichment: From present to deep-time. Earth Sci. Rev. 251, 104720. https://doi.org/10.1016/j.earscirev.2024.104720.

Liang, C., Wang, J.R., Cao, Y.C., Xiong, Z.H., Liu, K.Y., Hao, F., Han, W.L., 2024b. Authigenic calcite in shales: Implications for tracing burial processes and diagenetic fluid evolution in sedimentary basins. Earth Sci. Rev. 258, 104935. https://doi.org/10.1016/j.earscirev.2024.104935.

Lin, Z.Z., Li, J.Q., Wang, M., Zhang, P.F., Lu, S.F., Zhi, Q., Wang, J.J., Huang, H.S., 2022. Organic fluid migration in low permeability reservoirs restricted by pore structure parameters. J. Petrol. Sci. Eng. 218, 111028. https://doi.org/10.1016/j.petrol.2022.111028.

Lin, Z.Z., Hu, Q.H., Yin, N., Yang, S.Y., Liu, H.M., Chao, J., 2024a. Nanopores-to-microfractures flow mechanism and remaining distribution of shale oil during dynamic water spontaneous imbibition studied by NMR. Geoenergy Sci. Eng. 241, 213202. https://doi.org/10.1016/j.geoen.2024.213202.

Lin, Z.Z., Li, J.Q., Lu, S.F., Hu, Q.H., Zhang, P.F., Wang, J.J., Zhi, Q., Huang, H.S., Yin, N., Wang, Y., Ge, T.C., 2024b. The occurrence characteristics of oil in shales matrix from organic geochemical screening data and pore structure properties: An experimental study. Pet. Sci. 21 (1), 1–13. https://doi.org/10.1016/j.petsci.2023.09.002.

Loucks, R.G., Reed, R.M., Ruppel, S.C., Jarvie, D.M., 2009. Morphology, genesis, and distribution of nanometer-scale pores in siliceous mudstones of the Mississippian Barnett Shale. J. Sediment. Res. 79 (12), 848–861. https://doi.org/10.2110/jsr.2009.092.

Loucks, R.G., Reed, R.M., Ruppel, S.C., Hammes, U., 2012. Spectrum of pore types and networks in mudrocks and a descriptive classification for matrix-related mudrock pores. AAPG Bull. 96 (6), 1071–1098. https://doi.org/10.1306/08171111061.

Ma, L., Taylor, K.G., Lee, P.D., Dobson, K.J., Dowey, P.J., Courtois, L., 2016. Novel 3D centimetre-to nano-scale quantification of an organic-rich mudstone: The Carboniferous Bowland Shale, Northern England. Mar. Petrol. Geol. 72, 193–205. https://doi.org/10.1016/j.marpetgeo.2016.02.008.

Mathia, E.J., Bowen, L., Thomas, K.M., Aplin, A.C., 2016. Evolution of porosity and pore types in organic-rich, calcareous, lower Toarcian posidonia shale. Mar. Petrol. Geol. 75, 117–139. https://doi.org/10.1016/j.marpetgeo.2016.04.009.

Milliken, K.L., Curtis, M.E., 2016. Imaging pores in sedimentary rocks: Foundation of porosity prediction. Mar. Petrol. Geol. 73, 590–608. https://doi.org/10.1016/j.marpetgeo.2016.03.020.

Qian, Y.J., Gao, P., Fang, X.L., Sun, F.R., Cai, Y.D., Zhou, Y.F., 2022. Microstructure characterization techniques for shale reservoirs: A review. Front. Earth Sci. 10, 930474. https://doi.org/10.3389/feart.2022.930474.

Slatt, R.M., O'Brien, N.R., 2011. Pore types in the barnett and woodford gas shales: Contribution to understanding gas storage and migration pathways in fine-grained rocks. AAPG Bull. 95 (12), 2017–2030. https://doi.org/10.1306/03301110145.

Sondergeld, C.H., Ambrose, R.J., Rai, C.S., Moncrieff, J., 2010. Micro-structural studies of gas shales. SPE Unconventional Gas Conference, p. 131771. https://doi.org/10.2118/131771-MS.

Sun, Z.P., Wang, Y.L., Wu, B.X., Zhuo, S.G., Wei, Z.F., Wang, G., Xu, L., 2018. Chemical reactions and effects of slick water fracturing fluid on the pore structures of shale reservoirs in different deposition environments. J. Univ. Chin. Acad. Sci. 35 (5), 712–719. https://doi.org/10.7523/j.issn.2095-6134.2018.05.019 (in Chinese).

Tian, S.S., Guo, Y.L., Dong, Z.T., Li, Z.L., 2022. Pore microstructure and multifractal characterization of lacustrine oil-prone shale using high-resolution SEM: A case sample from natural Qingshankou Shale. Fract. Fract. 6, 675. https://doi.org/10.3390/fractalfract6110675.

Wang, B.J., Shi, B., Liu, Z.B., Cai, Y., 2004. Fractal study on microstructure of clayey soil by GIS. Chin. J. Geotech. Eng. 26, 244–247. https://doi.org/10.3321/j.issn:1000-4548.2004.02.018 (in Chinese).

Wang, X., Zhang, C., 2019. Quantitative characterization of shale organic pore space based on SEM. CT Theo. Appl. 28 (5), 519–527. https://doi.org/10.15953/j.1004-4140.2019.28.05.01 (in Chinese).

Wang, X.J., Wang, M., Li, Y., Zhang, J.X., Li, M., Li, Z., Guo, Z.Q., Li, J.B., 2021. Shale pore connectivity and influencing factors based on spontaneous imbibition combined with a nuclear magnetic resonance experiment. Mar. Petrol. Geol. 132, 105239. https://doi.org/10.1016/j.marpetgeo.2021.105239.

Wilkin, R.T., Barnes, H.L., 1997. Formation processes of framboidal pyrite. Geochem. Cosmochim. Acta 61 (2), 323–339. https://doi.org/10.1016/S0016-7037(96)00320-1.

Wilkin, R.T., Barnes, H.L., Brantley, S.L., 1996. The size distribution of framboidal pyrite in modern sediments: An indicator of redox conditions. Geochem. Cosmochim. Acta 60 (20), 3897–3912. https://doi.org/10.1016/0016-7037(96)00209-8.

Xia, D.B., Yang, Z.M., Gao, T.N., Li, H.B., Lin, W., 2021. Characteristics of micro-and nano-pores in shale oil reservoirs. J. Pet. Explor. Prod. 11, 157–169. https://doi.org/10.1007/s13202-020-01012-1.

Xiao, D.S., Zheng, L.H., Xing, J.L., Wang, M., Wang, R., Guan, X.D., Guo, X.Y., 2024. Coupling control of organic and inorganic rock components on porosity and pore structure of lacustrine shale with medium maturity: A case study of the Qingshankou formation in the southern Songliao Basin. Mar. Petrol. Geol. 164, 106844. https://doi.org/10.1016/j.marpetgeo.2024.106844.

Xu, L.L., Pan, R.F., Hu, H.Y., Meng, J.H., 2023. Contribution of various shale components to pore system: Insights from attributes analysis. J. Mar. Sci. Eng. 11 (7), 1327. https://doi.org/10.3390/jmse11071327.

Yang, R., He, S., He, J.Z., Hu, Q.H., 2016. Nano-scale pore structure and fractal dimension of organic-rich Wufeng-Longmaxi shale from Jiaoshiba area, Sichuan Basin: Investigations using FIB-SEM, gas adsorption and helium pycnometry. Mar. Petrol. Geol. 70, 27–45. https://doi.org/10.1016/j.marpetgeo.2015.11.019.

Yang, Y.M., Peng, J., Xu, T.Y., Wang, Y.B., Zeng, Y., 2022. Characterization, classification, and evaluation of the Reservoir Pore structure features of Lacustrine Fine-Grained Sedimentary Rocks. A case study of the Fourth Member of the Shahejie Formation in the Chenguanzhuang area of thesouthern gently sloping zone of the Dongying Sag, Bohai Bay Basin. Front. Earth Sci. 10, 878089. https://doi.org/10.3389/feart.2022.878089.

Zhang, L.Y., Chen, Z.H., Li, Z., Zhang, S.C., Li, J.Y., Liu, Q., Zhu, R.F., Zhang, J.G., Bao, Y.S., 2019. Structural features and genesis of microscopic pores in lacustrine shale in an oil window: A case study of the Dongying Sag. AAPG Bull. 103 (8), 1889–1924. https://doi.org/10.1306/1218181522717084.

Zhang, P.F., Lu, S.F., Li, J.Q., Wang, J.J., Zhang, J.J., Chen, G., Huang, H.S., Zhi, Q., Yin, Y.J., 2023. Microscopic characteristics of the pore-fracture system in lacustrine shale from Dongying Sag, Bohai Bay Basin, China: Evidence from scanning electron microscopy. Mar. Petrol. Geol. 150, 106156. https://doi.org/10.1016/j.marpetgeo.2023.106156.

Zhang, Q., Liu, Z.Y., Liu, C., Zhu, X.M., Steel, R.J., Tian, H.Y., Wang, K., Song, Z.P., 2021. Experimental study on the development characteristics and controlling factors of microscopic organic matter pore and fracture system in shale. Front. Earth Sci. 9, 773960. https://doi.org/10.3389/feart.2021.773960.

Yang, B., Qu, H.J., Pu, R.H., Tian, X.H., Yang, H., Dong, W.W., Chen, Y.H., 2020. Controlling effects of tight reservoir micropore structures on seepage ability: A case study of the Upper Paleozoic of the eastern Ordos Basin, China. Acta Geol. Sin-Engl. 94 (2), 322–336. https://doi.org/10.1111/1755-6724.14301.

Zhao, C.H., Wu, D., Hu, F.B., Sun, M., Li, T., Wang, H., 2023. Quantitative characteristics of micro bedding fractures in the Wufeng-Longmaxi Formation based on high-resolution map imaging technology. Processes 11 (7), 1942. https://doi.org/10.3390/pr11071942.

Zhao, W.Z., Zhu, R.K., Hu, S.Y., Hou, L.H., Wu, S.T., 2020. Accumulation contribution differences between lacustrine organic-rich shales and mudstones and their significance in shale oil evaluation. Petrol. Explor. Dev. 47 (6), 1160–1171. https://doi.org/10.1016/S1876-3804(20)60126-X.

Zou, C.N., Pan, S.Q., Jin, Z.H., Gao, J.L., Yang, Z., Wu, S.T., Zhao, Q., 2020. Shale oil and gas revolution and its impact. Acta Pet. Sin. 41, 1–12. https://doi.org/10.7623/syxb202001001 (in Chinese).